IX International Conference on Computational Methods in Marine Engineering
MARINE 2021
I.M. Viola and F. Brennan (Eds)

NOVEL MODELING METHODOLOGY OF THE DEEP-WATER FLEXIBLE RISER WITH THE SLUG-FLOW

MARINE 2021

HANZE YU*, YONGHE XIE*, GANGQIANG LI† AND LIJUN WANG*

* School of Naval Architecture and Maritime
Zhejiang Ocean University
316022 Zhoushan, Zhejiang, China
e-mail: s19082400001@zjou.edu.cn, xieyh@zjou.edu.cn, 421057262@qq.com

† Department of Mechanical Engineering
York University
M3J1P3 Toronto, Ontario, Canada
email: gangli@yorku.ca

Key words: Slug-flow, Flexible Riser, Arbitrary Lagrangian-Eulerian (ALE), Absolute Nodal Coordinate Formulation (ANCF)

Abstract. Slug flow, being the mixture of oil, gas and water, can increase the dynamics and structural response of a riser in internal fluid transportation due to the variation of slug flow's force caused by the time-space varying density. This paper presents a high-fidelity model of a flexible deep-water riser based on the absolute nodal coordinate formulation with slug flow in the arbitrary Lagrangian-Eulerian description. In the current paper, the Lagrangian and Eulerian description is introduced to describe the slug flow moving along the riser. Besides, a material coordinate is added together with the position and position gradient as the state variables. The riser is discretized into two types of elements, the constant-length and variable-length elements. The variable-length element is where the slug flow locates whose velocity of the material coordinates is equal to the slug flow speed, and its movement along the riser is simulated by the moving mesh technology. Considering the fact that the enormous ratio of the length to the riser's diameter, the Euler-Bernoulli beam theory is adopted to model the riser. In this paper, the equations of motion (EOM) of the riser subjected to the slug-flow and environmental loads are derived based on the generalized D'Alembert principle. The implicit time integration method is applied to solve the derived differential-algebraic equations. First, the proposed model and the slug flow method are validated. Second, Parametric studies are performed to quantitatively identify the design conditions most affected by the slug flow.

1 INTRODUCTION

The deep-water riser being the flexible component between a host platform and the subsea wellhead, plays a vital role in the gas exploration and oil production in offshore hydrocarbons. Slug-flow, a typical and complex flow pattern being the mixture of oil, gas and water inside the deep-water riser, occurs in internal fluid transportation. Due to the time-space varying density of slug-flow, the associated dynamic response affects the riser structure's stability, causing the potential fatigue failure.

The dynamic analysis of riser subjected to the internal slug-flow is still a challenging topic considering the mathematically modelling of the slug flow and the fluid-structure interactions. Monette [1] experimentally investigated the fluid-elastic instability behavior of a flexible tube subjected to the internal two-phase flow, whose results keep consistent with the modified model based on the existing theory and obtained experimental two-phase flow patterns. Ma [2] numerically predicted that the internal slug flow reduces the oscillation frequencies and triggers the multi-frequency and multi-modal interaction phenomenon at the high modes based on the dynamic analysis of a 2-D catenary riser. Furthermore, Wang [3] developed a dynamic model with a unified two-phase flow model and a modified model for the fluid-structure interaction system. The experimental and numerical results carried out by the dynamic response of horizontal pipes subjected to slug-flow imply that the slug-flow velocity affects the centrifugal and Coriolis forces, which causes intense vibration response of the riser.

The two-phase flow equation that describes the time-space varying density of slug-flow proposed by M.H. Patel [4] has been widely applied in the recent study on the dynamic response of the riser subjected to the internal slug-flow. Bai [5] employed the Bernoulli–Euler beam theory and the time-dependent density equation to investigate the dynamic behaviors of a cantilevered pipe system. They concluded that the system's complex frequency shows a periodic variation with the variation of the density. Furthermore, the cantilevered pipe system can easily lose its stability as the increasing of the fluctuating amplitude of the fluid density. The experiments performed by Zhu [6] illustrated that the multiple short slugs are present to dominate the unsteady behavior of the catenary riser as the gas-to-liquid flow rate is less than 2.5.

The study presented by Chatjigeorgiou [7] and the above-reviewed literature is classified as the Eulerian description. This description's primary consideration is the one-dimensional continuum medium's movement in the axial direction which is affected by the Coriolis force and the inertial entrainment force. In addition, the Eulerian description has a poor ability in handling the large deformation and rotation of the structure, which, in contrast, can be effectively solved by the Lagrangian description combined with the Absolute Nodal Coordinate Formulation (ANCF) mentioned in [8]. Thus, combining ANCF and the Arbitrary Lagrangian-Eulerian description (ALE), the latter of which is the combination of Lagrangian description and Eulerian description to capture the benefits of both descriptions while minimizing the disadvantages, is applied in this paper to address the large deformation and rotation problem of the deep-water riser subjected to internal slug-flow. As presented by Hong and Ren [9, 10], the ALE-ANCF based model has been investigated the transformed internal fluid inside a cable-type structure.

Concerning the strong ability of the ALE description to describe the characteristics of internal slug-flow and the ANCF to solve large deformation problem of flexible structures, in this paper, an ALE-ANCF based model is proposed to describe the internal slug-flow moving inside a cable and study the dynamic behaviors of a steel catenary riser (SCR) inclusive of an internal slug-flow. Section 2 describes the mathematical model of the riser containing the internal slug-flow in the framework of ALE-ANCF. In Section 3, based on the validation of the proposed model, the dynamic behavior of a steel catenary riser (SCR) subjected to the internal slug-flow is investigated. The slug-flow here is considered as a parcel of moving material in the partial riser with variable time-dependent density.

2 MATHEMATIC FORMULATION OF FLEXIBLE RISER SYSTEM SUBJECTED TO SLUG-FLOW IN FRAMEWORK OF ALE-ANCF

2.1 Description of the ALE-ANCF beam element

In terms of the enormous ratio of the length to the flexible riser's diameter, the ANCF approach, formulated by [11] has been adopted, where the riser is modeled by the Euler-beam theory. In addition, the arbitrary Lagrangian-Eulerian description is applied to describe the internal slug-flow contained in the beam element by introducing the material coordinates, as shown in **Figure 1**.

It can be seen from **Figure 1 (a)** and **(b)** that the beam element is defined by two sets of coordinate systems: the global fixed generalized coordinate system (*OXYZ*) and the element local coordinate system (*otnb*). As shown in **Figure 1 (a)**, the absolute position vector $\boldsymbol{r}$ of the ALE-ANCF beam element can be defined as,

$$\boldsymbol{r}(t)=\left[\boldsymbol{P}(t)^T,\boldsymbol{P}'(t)^T,u_1(t),u_2(t)\right]^T \tag{1}$$

where $\boldsymbol{P}(t)=(X_1,Y_1,Z_1,X_2,Y_2,Z_2)$ and $\boldsymbol{P}'(t)$ are the generalized global position vector and the absolute slope vector $\boldsymbol{r}'$ of the beam element, respectively. The superscript prime represents the derivative to the x-component of the position vector. $u_1(t)$ and $u_2(t)$ are the material coordinates of the head point and the endpoint of the beam element, respectively. The introduction of the material coordinates is used to control the internal slug-flow's movement by assigning speeds of material coordinates to the head point and the endpoint as $\dot{u}_1(t)$ and $\dot{u}_2(t)$ respectively. For instance, if $\dot{u}_1(t)=\dot{u}_2(t)>0$, the slug-flow element moves down. Otherwise, the fluid element moves upward or is fixed in its original position. In the current study, $\dot{u}_1(t)$ is considered equal to $\dot{u}_2(t)$.

According to the schematic diagram plotted in **Figure 1 (a)**, any point inside the i^{th} beam element can be expressed as,

$$\boldsymbol{r}(t)=\boldsymbol{N}_a\boldsymbol{P}_a \tag{2}$$

where $\boldsymbol{P}_a=\left[\boldsymbol{P}_i^T(t),\boldsymbol{P}_i'^T(t),\boldsymbol{P}_{i+1}^T(t),\boldsymbol{P}_{i+1}'^T(t)\right]^T$ is the elemental nodal coordinates of the i^{th} element. $\boldsymbol{N}_a$ is the global shape function matrix constructed by a Hermite interpolation function which has a complete set of rigid-body modes [9].

Besides, the local elemental frame is defined as shown in **Figure 1 (b)**. The tangential direction – *t*-axis is given by the straight line between the nodal points *i* and *i*+1 in the current configuration of element *i*. The positive direction of the *n*-axis is perpendicular to the *t*-axis and the elemental velocity vector. The *b*-axis completes a right-hand coordinate system.

Taking the first order and second-order time derivatives of the Eq. (1) yield,

$$\begin{aligned}\dot{\boldsymbol{r}}(t)&=\boldsymbol{N}_b\dot{\boldsymbol{P}}_b\\ \ddot{\boldsymbol{r}}(t)&=\boldsymbol{N}_b\ddot{\boldsymbol{P}}_b+\boldsymbol{h}_s\end{aligned} \tag{3}$$

where $\boldsymbol{N}_b=\left[\boldsymbol{N}_a\quad(\partial\boldsymbol{N}_a/\partial u_1)\boldsymbol{X}_a\quad(\partial\boldsymbol{N}_a/\partial u_2)\boldsymbol{X}_a\right]$ is the integrated shape function, and $\boldsymbol{h}_s$ is an equivalent acceleration term only influenced by the variation of material coordinates, seen in [9].

2.2 Finite element discretization of the riser-slug-flow system

Consider the flexible hanging riser shown in **Figure 2** being subjected to the internal upward slug-flow with variable time-dependent density and the external uniformly current. The equations of motion (EOM) of the mass-varying system are derived from the generalized D'Alembert principle. For the i^{th} element again, its virtual work can be written as,

$$\delta W = \delta W_{elastic} + \delta W_{inertial} + \delta W_{external} = 0 \tag{4}$$

where δ is the variational operator. δW denoting the virtual work done by the sum of the forces with subscripts *elastic*, *inertial*, and *external* representing the elastic, inertial, and external forces, respectively. The items aforementioned are given as follows,

$$\begin{aligned}
\delta W_{elastic} &= -\delta \boldsymbol{P}_{b,i}^T \frac{L_{e,i}}{2} \int_{-1}^{1} \left(E_i A_i \bar{\varepsilon}_l \left(\frac{\partial \varepsilon}{\partial \boldsymbol{P}_{b,i}} \right)^T + E_i I_i \left(\frac{\partial \kappa}{\partial \boldsymbol{P}_{b,i}} \right)^T \kappa \right) ds \\
\delta W_{inertial} &= -\delta \boldsymbol{P}_{b,i}^T \left(\boldsymbol{M}_{b,i} \ddot{\boldsymbol{P}}_{b,i} + \frac{L_{e,i}}{2} \int_{-1}^{1} \left(\rho_i A_i + \rho_{fluid} A_{fluid} \right) \boldsymbol{N}_{b,i}^T \boldsymbol{h}_s ds \right) \\
\delta W_{external} &= \delta \boldsymbol{P}_{b,i}^T \frac{L_{e,i}}{2} \int_{-1}^{1} \boldsymbol{N}_{b,i}^T \boldsymbol{f}_{external,i} ds
\end{aligned} \tag{5}$$

where $L_{e,i} = u_2 - u_1$ is the length of the i^{th} element. $\bar{\varepsilon}_l = \left(L_{elastic} - L_{e,origin} \right) / L_{e,origin}$ is approximately evaluated based on the small deformation assumption, with $L_{elastic} = \sqrt{\left(X_i - X_{i+1} \right)^2 + \left(Y_i - Y_{i+1} \right)^2 + \left(Z_i - Z_{i+1} \right)^2}$ being the deformed length of the element. E_i, A_i, I_i, and ρ_i are the elastic module, cross-section area of the beam, second-moment inertia, and the density of the structure element, respectively. In addition, $(\ )_i$ represents the i^{th} element. ρ_{fluid} and A_{fluid} mean the variable time-dependent density of internal slug-flow and the cross-section area of internal flow, the detailed expression of the former refers to [4]. κ is the bending curvature, seen in [9]. $\boldsymbol{f}_{erternal}$ is the sum of the gravity, current dray force, and buoyancy of the i^{th} element, respectively.

Substituting Eq. (5) into Eq. (4) yields,

$$\boldsymbol{M}_{b,i} \ddot{\boldsymbol{P}}_{b,i} + \boldsymbol{K}_{b,i} \boldsymbol{P}_{b,i} + \boldsymbol{F}_{\boldsymbol{hs},i} = \boldsymbol{F}_{external,i} \tag{6}$$

Where $\boldsymbol{M}_{b,i}$ $\boldsymbol{K}_{b,i}$, $\boldsymbol{F}_{external,i}$, and $\boldsymbol{F}_{\boldsymbol{hs},i}$ are the time-dependent mass matrix, stiffness matrix, the external forces vector and the additional inertial force caused by the fluid-structure interaction of the i^{th} element, respectively. The detailed presentations of the external forces are shown in the following sections. After that, the dealing of the constraints of the riser-slug-flow system and the time integration scheme are carried out.

2.3 Gravity evaluation

The gravity per unit length is calculated as,

$$\boldsymbol{f}_{gravity} = \left[0, 0, -\left(\rho_i A_i + \rho_{fluid} A_{fluid} \right) g \right]^T \tag{7}$$

where g = 9.81 m/s^2 is the constant gravitational acceleration.

2.4 Current drag force evaluation

The current darg force per unit length can be evaluated as,

$$\boldsymbol{f}_{drag}^{g} = \boldsymbol{T}_{l2g}\,\boldsymbol{f}_{drag}^{l} \tag{8}$$

where $\boldsymbol{T}_{l2g} = \boldsymbol{T}_{g2l}^{T}$ is the transform matrix from the elemental local frame to the global frame refers to [12] and [13]. The detailed formulation of the current drag force refers to [14].

2.5 Buoyancy evaluation

The buoyancy per unit length is calculated as,

$$\boldsymbol{f}_{buoyanvy} = \left[0, 0, \rho_w g A_{ext}\right]^T \tag{9}$$

where ρ_w and A_{ext} are the water density and the cross-section area formulated by the external diameter, respectively.

2.6 Equations of motion of the riser

The equations of motion (EOM) of the riser-slug-flow system is obtained by assembling all elements in the finite element method, seen in [15],

$$\boldsymbol{M}_b\ddot{\boldsymbol{P}}_b + \boldsymbol{K}_b\boldsymbol{P}_b + \boldsymbol{F}_{\boldsymbol{hs}} = \boldsymbol{F}_{external} \tag{10}$$

where $\boldsymbol{M}_b$ and $\boldsymbol{K}_b$ are the mass and stiffness matrixes of the riser system, respectively. $\boldsymbol{P}_b$ is the generalized global coordinates of the riser system. $\boldsymbol{F}_{external}$ and $\boldsymbol{F}_{\boldsymbol{hs}}$ are the force vectors acting on the riser.

2.7 Constraint equations

In this study, the constraint equations are divided into two types. One is the constraints of the material coordinates, and the other is the riser's boundary condition used to connect the upper platform and the bottom wellhead. The constraints of the material coordinates can be categorized into the fixed material coordinate type and the moving material coordinate type, as plotted in **Figure 3**.

As shown in the **Figure 3**, the black nodes represent the fixed material coordinates, indicating the nodes' material coordinates keep constant. The constraint equations can be written as,

$$\boldsymbol{C}_1 = \boldsymbol{0} \Leftrightarrow \left\{u_i - u_{i,ini} = 0,\ \left(i = 1, 2, \cdots, k-2, k+1, \cdots, n, n+1\right)\right. \tag{11}$$

where $(\ )_{ini}$ means the value of material coordinates at the very beginning. For the structural element with moving internal slug-flow, the material coordinates at the initial time are indicated by the yellow nodes, and the blue nodes correspond to the moving material coordinates after a while. Note that the moving material coordinates shown in the specific illustration diagram of **Figure 3** move at the same speed in the interval from node *k*-2 to node *k*+2. Thus, the constraint equations of the moving material coordinates can be written as,

$$\boldsymbol{C}_2 = \boldsymbol{0} \Leftrightarrow \left\{u_i - u_{i,pres} = 0\left(i = k-1, k, k+1\right)\right. \tag{12}$$

where $u_{i,pres} = u_{i,ini} + \dot{u}_{i,pres}\Delta t\left(i = k-1, k, k+1\right)$. $u_{i,ini}$ is the material coordinates at the initial time, $\dot{u}_{i,pres}$ is the speed of the internal moving fluid, and Δt is the time step in the calculation.

As for the boundary conditions of the riser system, the constraint equations can be given as,

$$\boldsymbol{C}_3 = \boldsymbol{0} \Leftrightarrow \boldsymbol{P}_i - \boldsymbol{P}_{i,ini} = \boldsymbol{0}\left(i = 1, n+1\right) \tag{13}$$

2.8 Time integration scheme

The differential-algebraic equations (DAEs) can be obtained by Combining the Eqs. (10)-(13) with the Lagrangian multiplier method,

$$\begin{cases} \boldsymbol{M}_b \ddot{\boldsymbol{P}}_b + \boldsymbol{K}_b \boldsymbol{P}_b = \boldsymbol{F}_{external} + \boldsymbol{F}_{hs} + \sum_{m=1}^{3} \boldsymbol{J}_m^T \boldsymbol{\lambda}_m = \boldsymbol{0} \\ \boldsymbol{C}_1\left(\boldsymbol{P}_b, t\right) = \boldsymbol{0} \\ \boldsymbol{C}_2\left(\boldsymbol{P}_b, t\right) = \boldsymbol{0} \\ \boldsymbol{C}_3\left(\boldsymbol{P}_b, t\right) = \boldsymbol{0} \end{cases} \tag{14}$$

where $\boldsymbol{\lambda}_m$ are the Lagrangian multipliers, and $\boldsymbol{J}_m = \partial \boldsymbol{C}_m / \partial \boldsymbol{P}_b$ is the Jacobian matrix of the constraint equations with respect to the state vector.

The backward Eulerian scheme is used to discretize the Eq. (14) in time, seen in [16]. After that, the Newton-Raphson iterative algorithm is applied to solve the formula numerically [17]. The iteration solver's accuracy is controlled by the residual error and maximum iteration number. Their values will be given in the following part, respectively.

3 NUMERICAL CASES STUDY

The mathematical formulation introduced above has been implemented into a Fortran code. Numerical results of two cases are performed to verify the proposed model's implementation by comparing with those obtained by a commercial finite element software – ProteusDS. Then, the dynamic response of a steel catenary riser (SCR) subjected to the internal slug-flow is investigated. The calculation convergence error and the iteration solver's maximum iteration number are set to be 1×10^{-10} and 100, respectively.

3.1 Case 1: A free-falling elastic beam in the air

A free-falling elastic beam in the air, as shown in **Figure 4**, is firstly set up to validate the implementation of the ALE-ANCF model under gravity. One end of the elastic beam (head point) is initially connected to a pin joint in the air, limiting the beam's translation in the global frame, while the other end (endpoint) is set to be free. The beginning configuration of the elastic beam is horizontal with zero velocity.

Note that all the nodes' nodal material coordinates are uniformly distributed and kept fixed, seen Eq. (11). This procedure aims to ensure the results produced by ALE-ANCF stay consistent with conventional ANCF with mesh nodes fixed. The elastic beam's physical parameters are retrieved from [11]. The standard gravitational acceleration and the time step are 9.81 m/s^2 and 0.0001 s, respectively. For examining the accuracy of the proposed 14-degrees-of-freedom ALE-ANCF program, the results produced by our code are compared with those obtained by ProteusDS using the same physical and simulated parameters.

A sensitivity study is first conducted to choose the proper elements' number for simulations. Four different element division schemes are applied. The comparison of results is shown in **Figure 5 (a)**. It is evident that the results obtained from these four schemes match well with no significant differences. In terms of the proposed program's efficiency, 12 elements are selected for the subsequent comparison.

Figure 5 (b) shows the time traces of the vertical position of the elastic beam's free end. It can be viewed that the results between the ALE-ANCF model and ProteusDS agree well.

Because of the adoption of the different finite elements models [18], there is a slight difference during the ascent of the free end from 0.53 s to 1.05 s. To get a visual comparison, **Figure 6** compares the configurations between the current implemented method with those obtained by ProteusDS at every 0.1 s time interval. In general, the contrasts prove that our model results keep consistent with those from Proteus.

3.2 Case 2: Comparison of the static configurations of steel catenary riser (SCR)

In this section, the more complex external environmental loads, including buoyancy and current drag force, are considered to validate the proposed model's consistency and accuracy. Besides, a more realistic hanging SCR is adopted to validate the applicability of our code. The physical parameters of the SCR are taken from [19], and 12 elements are used to discrete the riser structure suggested by the sensitivity study. Different from other literature did [20], in this case, the SCR is assumed to be subjected to a uniform current flow with a speed of 1 m/s as shown in **Figure 2**. Note that $C_D^n = 1$ and $C_D^t = 0$.

The constant gravitational acceleration is 9.81 m/s^2 and the simulation time step chosen to be 0.0001 s. **Figure 7** shows that the static configurations produced by the present model and ProteusDS are very close. In summary, the above two numerical results show that the proposed ALE-ANCF model is reasonable and capable of dealing with the following complicated dynamic simulation of SCR subjected to the moving internal slug-flow.

3.3 Case 3: Dynamic analysis of SCR subjected to upward slug-flow

The internal slug-flow is applied to the SCR in case 2 to investigate the influences of internal slug-flow on the flexible riser's vibration response. It should be pointed that only the partial riser contains the internal slug-flow. The more detailed related parameters can be referred to [20].

Based on the static configuration obtained in case 2, the same environmental loads are applied to the SCR for dynamic analysis. For this case, the internal slug-flow is supposed to be contained in a segment of SCR as plotted in **Figure 8 (a)**. The simulation time is set to be 350 s, where the first 200 s is used to obtain the stable dynamic configurations of SCR without the movement of internal slug-flow. Subsequently, the internal slug-flow controlled by the velocities of the material coordinate of nodes 6, 7, 8 moves upward at the speed of 0.1 m/s during the following 150 s inside the SCR. The moving upward slug-flow is realized by assigning the material coordinates of nodes 6, 7, 8 as the equivalent speed. In other words, the rate of upward internal slug-flow is equal to that of the material coordinates of nodes 6, 7, 8.

Unlike case 1, each SCR structure node's material coordinate is not uniformly distributed in this case as shown at the beginning of **Figure 9**, which displays the time variation of material coordinates of the 13 nodes on the SCR. The whole SCR structure nodes are divided into two parts: three moving nodes 6, 7, 8 with the same speed, and the remaining ten material coordinate fixed nodes. The initial material lengths of the elements between the three moving nodes and the ten fixed nodes are 20 m and 12 m, respectively. In addition, the material length between node 8 and 9 is set as 12 m, shorter than that between node 5 and node 6 of 22 m. The setting of simulation time and material lengths mentioned above is to ensure the conduct of the numerical simulation, which can be influenced by the variable material lengths due to the movement of internal slug-flow. The time variation of material coordinates of 13 nodes on

the SCR from 200 s to 350 s demonstrates the aforementioned setting is performed correctly. The schematic diagram of constraints of material coordinates is displayed in **Figure 3**.

In **Figure 8 (b)**, the dynamic configurations of SCR subjected to internal slug-flow with variable time-dependent density are displayed. Different color curves represent SCR configurations at moments 190 s, 250 s, and 300 s under the respective corresponding condition. The results show that the SCR configurations change significantly with the movement of the internal slug-flow – the configuration at the moment 300 s is more drastic than that at 250 s. For instance, as the internal slug-flow moving up, the trajectories of nodes 6 and 7 move to the upper left gradually, with nodes 8 and 9 shifting to a lower place. Interestingly, the displacement variation of node 8 is much smaller than that of nodes 6, 7, and 9, making this segment of SCR seems to turn counterclockwise with node 8 as the center. The reason for this phenomenon is that the upward moving of the internal slug-flow is actually realized by assigning the material coordinate velocities to nodes 6, 7, 8, which corresponds to the introduction of an additional force pushing these two fluid elements upward, causing the top half of the SCR nodes to the upper left while the latter half nodes move to the lower place.

To further reveal the impact of the upward internal slug-flow on the dynamic response of SCR, the SCR subjected to an upward internal flow with a constant density equal to 449.605 kg/m^3 is simulated. The same setting as mentioned above is applied to this simulation. The comparisons of displacement time histories in the horizontal direction and vertical direction of SCR subjected to the internal slug-flow with variable density and upward flow with constant density at node 7 are plotted in **Figure 10**. It can be seen that both simulations already obtain the stable dynamic configurations before the upward movement of the internal fluid from 150 s to 200 s. For the beginning of 200 s, both simulations' horizontal and vertical positions of node 7 variate in the same direction, respectively. However, as can be observed from the small plot on the right hand in **Figure 10 (a)** and **(b)**, the differences between the two simulations can not be ignored. The vibration amplitude of node 7 in the case of being subjected to the internal slug-flow is more significant than that of being subjected to the upward flow with constant density. In addition, the variation of nodes 6, 7 and 9 in the horizontal and vertical directions are much greater than that of node 8 which echoes the variation of displacement of node 8 in **Figure 8 (b)** mentioned above. This phenomenon indicates that the internal slug-flow with variable time-dependent density can generate a superposition of the structure deformation, aggravating the SCR oscillates.

4 CONCLUSION

In this study, a novel modelling methodology of the deep-water flexible riser subjected to internal slug-flow is developed based on the combination of the absolute nodal coordinate formulation (ANCF) and the arbitrary Lagrangian-Eulerian (ALE) description. In the framework of ALE-ANCF, the characteristics of slug-flow can be easily described by the introduction of material coordinates, which is the benefit brought by ALE description. In addition, the application of ANCF enables the proposed model to have the great abilities to handle the large deformation and large rotation of the deep-water flexible riser. First, the accuracy of the developed model is validated by comparing results of the dynamic response of a free-falling elastic beam under gravity and the static configuration of a hanging steel

catenary riser (SCR) subjected to the buoyancy and uniform current with those obtained by ProteusDS. The comparison results show that the proposed methodology is acceptable and accurate. Then, based on the static configuration obtained in case 2, a realistic hanging SCR conveying the internal upward slug-flow is conducted, whose results present the dynamic configurations of the SCR-slug-flow system is reasonable and acceptable. The significant variation of the configurations implies that the internal slug-flow generates a superposition to the structural deformation that impacts the hanging SCR's motion.

REFERENCES

[1] Monette, C. and M.J. Pettigrew, Fluidelastic instability of flexible tubes subjected to two-phase internal flow. *J. Fluids. Struct* (2004). **19**(7): 943-956.

[2] Ma, B. and N. Srinil. Dynamic characteristics of deep-water risers carrying multiphase flows. 2018. *Proceedings of the ASME 2018 37th International Conference on Ocean, Offshore and Arctic Engineering OMAE2018, 17-22 June 2018, Madrid, Spain. OMAE2018- 51241*.

[3] Wang, L., et al., Dynamic behaviours of horizontal gas-liquid pipes subjected to hydrodynamic slug flow: Modelling and experiments. *Int. J. Pres. Ves. Pip* (2018). **161**: 50-57.

[4] Patel, M.H. and F.B. Seyed, Internal flow-induced behaviour of flexible risers. *Eng. Struct* (1989). **11**(4): 266-280 .

[5] Bai, Y., et al., Dynamic analysis of a cantilevered pipe conveying fluid with density variation. *J. Fluids. Struct* (2018). **81**: 638-655.

[6] Zhu, H., et al., Mode switching and standing-travelling waves in slug flow-induced vibration of catenary riser. *J. Petrol. Sci. Eng* (2021). **203**: 108310.

[7] Chatjigeorgiou, I.K., On the effect of internal flow on vibrating catenary risers in three dimensions. *Eng. Struct* (2010). **32**(10): 3313-3329.

[8] Belytschko, T., et al., *Nonlinear finite elements for continua and structures*. 2013: John wiley & sons.

[9] Hong, D.F. and G.X. Ren, A modeling of sliding joint on one-dimensional flexible medium. *Multibody. Syst. Dyn* (2011). **26**(1): 91-106.

[10] Hong, D.F., J.L. Tang, and G.X. Ren, Dynamic modeling of mass-flowing linear medium with large amplitude displacement and rotation. *J. Fluids. Struct* (2011). **27**(8): 1137-1148.

[11] Berzeri, M. and A.A. Shabana, Development of Simple Models for the Elastic Forces in the Absolute Nodal Co-Ordinate Formulation. *J. Sound. Vib* (2000). **235**(4): 539-565.

[12] Li, G.Q. and Z.H. Zhu, Long-term dynamic modeling of tethered spacecraft using nodal position finite element method and symplectic integration. *Celest. Mech. Dyn. Astr* (2015). **123**(4): 363-386.

[13] Li, G. and Z.H. Zhu, Multiphysics finite element modeling of current generation of bare flexible electrodynamic tether. *J. Propul. Power* (2017). **33**(2): 408-419.

[14] Takehara, S., Y. Terumichi, and K. Sogabe, Motion of a submerged tether subject to large deformations and displacements. *Journal of System Design and Dynamics* (2011). **5**(2): 296-305.

[15] Li, G., Z.H. Zhu, and C. Du, Flight dynamics and control strategy of electric solar wind sails. *J. Guid. Control. Dynam* (2020). **43**(3): 462-474.
[16] Li, G. and Z.H. Zhu, On libration suppression of partial space elevator with a moving climber. *Nonlinear. Dynam* (2019). **97**(4): 2107-2125.
[17] Li, G., Z.H. Zhu, and C. Du, Stability and control of radial deployment of electric solar wind sail. *Nonlinear. Dynam* (2021). **103**(1): 481-501.
[18] Buckham, B., F.R. Driscoll, and M. Nahon, Development of a finite element cable model for use in low-tension dynamics simulation. *J. Appl. Mech* (2004). **71**(4): 476-485.
[19] Low, Y.M. and R.S. Langley. Dynamic analysis of a flexible hanging riser in the time and frequency domain. *Proceedings of the ASME 2006 25th International Conference on Ocean, Offshore and Arctic Engineering OMAE2006, 4-9 June 2006, Hamburg, Germany. OMAE2006-92171.*
[20] Chen, H., S. Xu, and H. Guo, Nonlinear analysis of flexible and steel catenary risers with internal flow and seabed interaction effects. *J. Mar. Sci. Eng* (2011). **10**(2): 156-162.

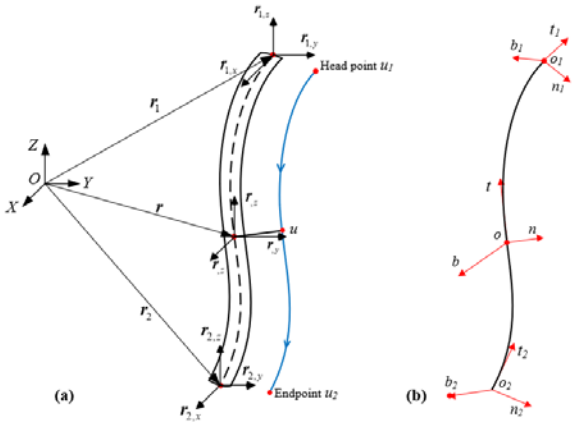

Figure 1: Configuration of a beam element in the **(a)** global frame and **(b)** element local frame

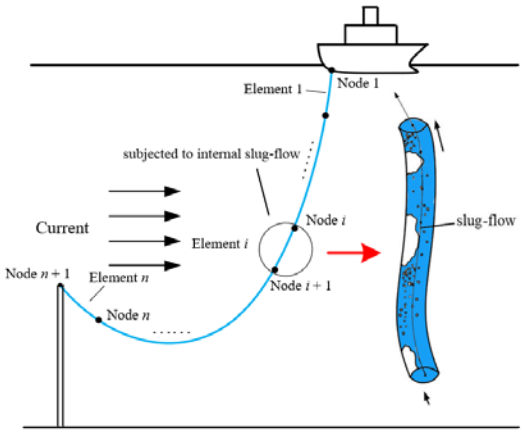

Figure 2: Schematic diagram of a flexible riser subjected to external uniform current and internal slug-flow

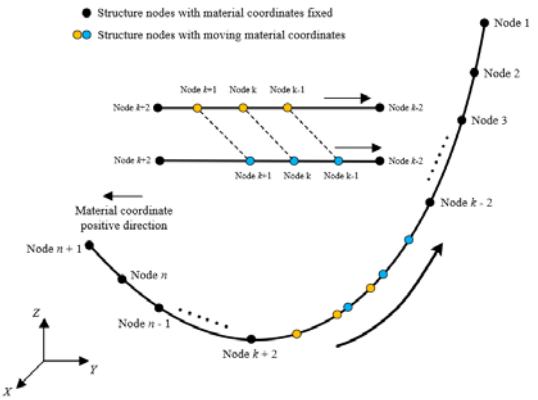

Figure 3: The schematic diagram of constraints of material coordinate of the riser-slug-flow system

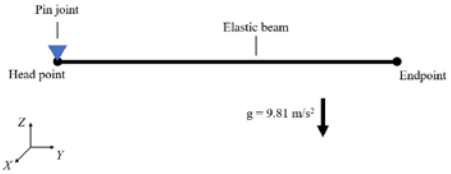

Figure 4: The schematic diagram of a free-falling elastic beam in the air ignoring the air resistance

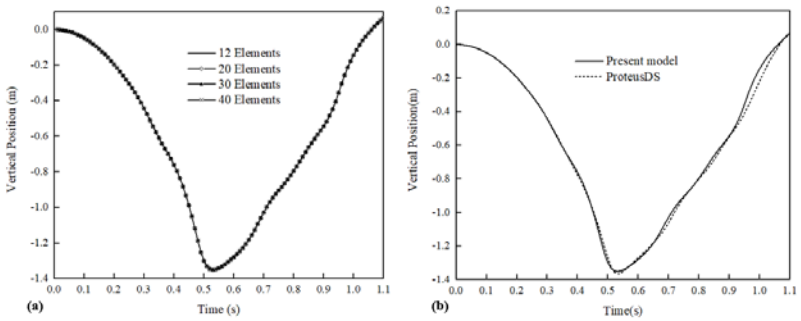

Figure 5: **(a)** The number of elements that impact the dynamic response of the elastic beam **(b)** Comparison results of time variation vertical position of the free endpoint of the elastic beam between the present model and ProterusDS

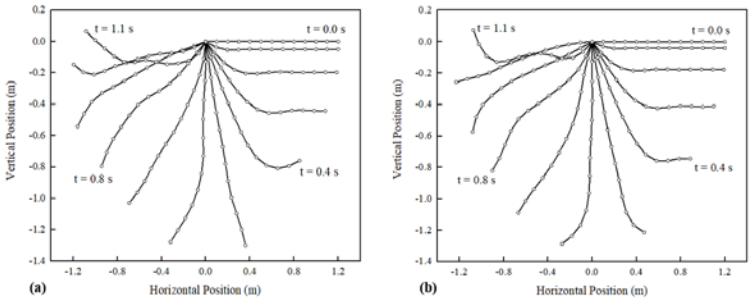

Figure 6: Comparison results of time variation configurations of the free-falling elastic beam between **(a)** present model (ALE-ANCF) and **(b)** ProteusDS at every 0.1 s interval

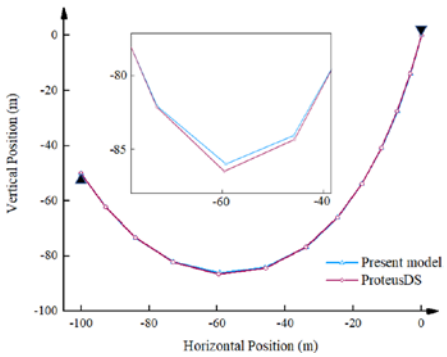

Figure 7: Static configurations obtained by the present ALE-ANCF model and ProteusDS

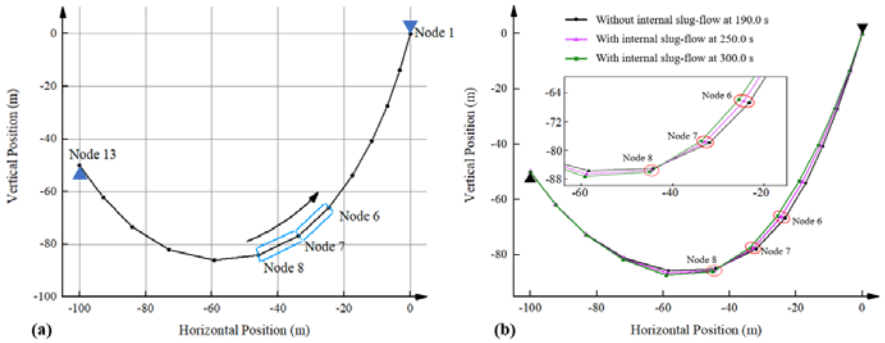

Figure 8: **(a)** Schematic diagram of the static configuration of SCR subjected to internal slug-flow **(b)** Dynamic configurations of SCR subjected to internal slug-flow with variable time-dependent density at moments 190 s, 250 s, and 300 s

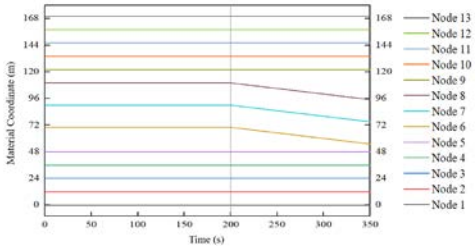

Figure 9: Time variation of material coordinates of the 13 nodes on the SCR

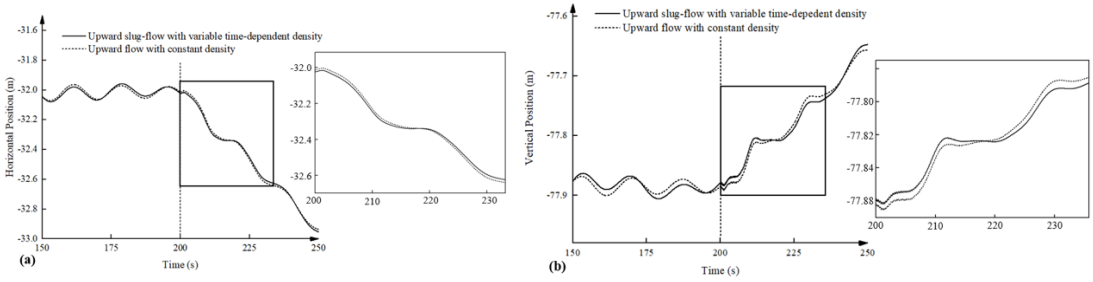

Figure 10: Comparisons of the displacement time history of SCR subjected to the slug-flow with variable density and upward flow with constant density in **(a)** Horizontal direction and **(b)** Vertical direction of node 7